A non-homogeneous constitutive model for human blood. Part III. Oscillatory Flow

Miguel A. Moyers-Gonzalez [1] and Robert G. Owens [2]

Département de mathématiques et de statistique, Université de Montréal, CP 6128 succ. Centre-Ville, Montréal QC H3C 3J7, Canada.

Jiannong Fang

GEOLEP-ICARE-ENAC, Ecole Polytechnique Fédérale de Lausanne, 1015 Lausanne, Switzerland.

Abstract

Numerous experiments have been performed that show that for oscillatory blood flow in a tube, sufficiently large volume flow rate amplitudes will break up blood aggregates leading to a loss of elasticity and to a response by the pressure gradient oscillations typical of those of a viscous fluid in inertial flow [G. B. Thurston, Elastic effects in pulsatile blood flow, Microvasc. Res. 9 (1975), 145-157]. In this paper we use the non-homogeneous blood model developed in Part I of this work [M. Moyers-Gonzalez, R. G. Owens and J. Fang, A non-homogeneous constitutive model for human blood. Part I: Model derivation and steady flow (2007), under review] to simulate blood undergoing oscillatory flow and, in particular examine the behaviour of the components of the pressure gradient that are in phase and $\pi/2$ out of phase with the volume flow rate, as the volume flow rate amplitude is varied. Excellent agreement is found with experimental data for a tube of radius $430\mu m$. An improvement in the predictions compared to those of an earlier homogeneous model [J. Fang and R. G. Owens, Numerical simulations of pulsatile blood flow using a new constitutive model, Biorheology 43 (2006) 637–660] is evidenced. We also seek to relate the macroscopic blood behaviour in different size tubes and at two different angular frequencies to the aggregate properties such as the average aggregate size and the cell number density.

Key words: Non-homogeneous fluid, oscillatory flow, aggregates, blood.

[1] Present address: Department of Mathematical Sciences, University of Durham, Science Laboratories, South Road, Durham DH1 3LE, UK

[2] Corresponding author. Email: owens@dms.umontreal.ca

1 Introduction

Within the heart and the aorta of the human cardiovascular system it is generally accepted that blood may be considered as a Newtonian fluid and therefore described adequately by the Navier-Stokes equations [14]. In a recent image-based CFD study of blood flow through the carotid bifurcation it was found that, for example, wall shear stress values were far less sensitive to rheological changes in blood than to geometric uncertainty and the conclusion of the authors was that, given the currently available levels of geometric precision in experiments (despite the obvious progress in flow imaging over the last decade [24]), even in these smaller arteries (of diameter c. $5mm$ [5]) a simple rescaling of the Newtonian viscosity was sufficient to take account of non-Newtonian behaviour [16].

In yet smaller vessels, however, a knowledge of the non-Newtonian rheology becomes essential to a correct understanding of its flow properties. In its passage between the smallest arteries and the capillary bed and in glass tubes of diameters in this range, it has been known for some considerable time that blood is shear-thinning, viscoelastic and thixotropic (see, for example, [25]), due mainly to the behaviour of the red blood cells in suspension. One of the commonest ways in which the non-Newtonian character of oscillatory blood flow in small vessels and tubes has been demonstrated in the literature is by considering the pressure gradient-volume flow rate relationship.

Suppose that the volume flow rate U of a fluid undergoing sinusoidal motion with angular frequency ω in a uniform rigid-walled right cylindrical tube may be written in the form

$$U = U_M \cos \omega t = \frac{\omega}{2} V_s \cos \omega t, \tag{1}$$

for some real flow rate amplitude $U_M = \omega V_s/2$, where V_s is a stroke volume. Denoting the pressure drop per unit length in the axial direction by $P = -\partial p/\partial z$ we further suppose that P and U are related through an equation of the form

$$P = \mathfrak{Re}(Z U_M \exp(i\omega t)). \tag{2}$$

In (2) $\mathfrak{Re}$ denotes that the real part is taken and $Z \in \mathbb{C}$ is the hydraulic impedance, which may be written as the sum of its real and imaginary parts as

$$Z = R + iX,$$

where $R, X \in \mathbb{R}$ are called, respectively, the hydraulic resistance and the hydraulic reactance. In general, we may write P in the form

$$P = \mathfrak{Re}((P'_M + iP''_M) \exp(i\omega t)), \tag{3}$$

where P'_M and P''_M are, respectively, the in phase and quadrature components of P. Therefore, equating (2) and (3) we have that

$$R = \frac{P'_M}{U_M} \text{ and } X = \frac{P''_M}{U_M}. \tag{4}$$

By analogy with the definition of the apparent viscosity of blood undergoing steady Poiseuille flow a dynamic apparent viscosity (or *equivalent* viscosity [7]) may be defined as the viscosity of a Newtonian fluid exhibiting the same amplitudes of pressure gradient and volume flow rate at a given frequency.

In [15] Kunz and Coulter considered the sinusoidal oscillatory flow of blood at various hematocrits and of an aqueous glycerol solution in a rigid tube of radius $1.7mm$. The stroke volume V_s was fixed at $0.204cc$, so that from (1) it may be seen that as the frequency ω of the oscillations varied, so did the volume flow rate U. It was found that although the hydraulic reactance X of 47% hematocrit blood differed little from the prediction of the Womersley solution [33] for a Newtonian fluid of comparable viscosity, the hydraulic resistance differed significantly from the Newtonian prediction, decreasing (rather than increasing) with increasing frequency and eventually passing through a minimum before increasing again at higher frequencies. The dynamic apparent viscosity decreased for all hematocrits as a function of frequency. But since higher frequencies meant higher volume flow rate amplitudes it was not clear from the Kunz and Coulter paper to what extent the dynamic apparent viscosity depended on frequency and to what extent on flow rate. The behaviour of the dynamic apparent viscosity with increasing oscillatory frequency in [15] was interpreted some four years later by Coulter and Singh [7] as being due to the higher shear rates at higher frequencies experienced by the fluid. In the Coulter and Singh paper [7] the authors decoupled the flow rate and frequency by performing experiments in rigid-walled tubes at various frequencies but at fixed flow amplitudes. The tube radii ranged from $0.304mm$ to $1.62mm$. This time the dynamic apparent viscosity of 40% hematocrit blood increased in tubes of all radii as a function of oscillatory frequency. At any given frequency the dynamic apparent viscosity increased with tube radius. Once again, although the hydraulic reactance was well predicted by the Womersley theory, the measured hydraulic resistance for the blood was significantly larger than the theoretical Newtonian value at the highest frequencies. The same trend had already been observed experimentally by Fry et al. [12] in *in vivo* experiments performed on the descending thoracic aorta of dogs. It should be remarked at this point that attributing all discrepancies between the Womersley predictions in [33] and measured quantities described above to the non-Newtonian character of blood alone is complicated by the fact that Womersley made assumptions in the derivation of his theoretical model that went beyond simply assuming the fluid to be Newtonian. These included the neglect of the nonlinear inertial terms in the equation of motion, axisymmetry of the flow, a non-tapered long vessel having circular cross-section, the walls

of which did not pulsate greatly.

Some time later Thurston [28,29] studied the steady, oscillatory and pulsatile flow of blood in tubes of various radii and, in particular, presented results showing how the in-phase and quadrature components of the pressure gradient behaved as functions of the volume flow rate amplitude. Earlier work by Thurston [27] had led to explicit expressions for the two pressure gradient components in the case of oscillatory flow of a linear viscoelastic fluid at small ($\ll 1$) Womersley numbers. In the case of blood, by identifying P'_M with an energy dissipative component and P''_M with a recoverable energy component the variation of the two components with U_M demonstrated how the viscosity and elasticity varied with volume flow rate amplitude in the case of the unsteady flows considered. In oscillatory flow, as the volume flow rate amplitude increased and blood aggregates began to break up, the blood was seen to lose its elasticity and the response of the pressure gradient oscillations became those of a viscous fluid in inertial flow. Oscillatory flow experiments by Vlastos et al. [31] with and without an imposed steady shear flow demonstrated that as the shear strain amplitude increased both the viscous and elastic components of the complex viscosity decreased, with the elastic component showing a sharper decrease than that observed in the viscous component.

Despite the plethora of papers on numerical simulations of oscillatory or pulsatile blood flow in the scientific literature, there have been comparatively few attempts to predict the changing viscous and elastic properties of blood in oscillatory flow using models that are viscoelastic. Among the few examples of realistic viscoelastic constitutive models for blood that have been developed we here cite those of Yeleswarapu [34,35] and of Anand and Rajagopal [1], the latter model being developed within the general thermodynamic framework established in [21]. Anand and Rajagopal's model gave good agreement with the experimental results of Thurston [28] in both steady and oscillatory blood flow in straight tubes and comparison was also made with the Yeleswarapu model. Generalized Oldroyd B and Maxwell models (also developed from [21]) were found to be inadequate for describing oscillatory flow. In 2006, Fang and Owens [11] used the homogeneous blood model of Owens [20] to simulate the same flows treated experimentally by Thurston [28], but with the parameter set chosen a slip boundary condition had to be introduced in order to correctly predict the crossover point of P''_M as a function of oscillatory volume flow rate amplitude from negative to positive. In Section 4.2 of this paper we re-evaluate the homogeneous model using a more realistic parameter set. In particular, the zero shear-rate steady viscosity is chosen to be smaller than in [11] and no artificial slip condition is needed. Even more recently, in Part I of this work, Moyers-Gonzalez et al. [17] have described a non-homogeneous blood model, that predicts particle migration away from vessel walls and thus allows for a cell depleted slip layer to develop there. In the present paper we use this model in the numerical simulation of oscillatory blood flow and the

improvement of the results over those obtained with the simpler model of Fang and Owens [11] demonstrates the importance of wall effects in tubes of the size considered.

Section 2 of this paper is recapitulative and summarizes from Part I of this work [17] the model equations and the boundary conditions appropriate for tube flow. A simple second-order finite element method for the solution of the equation set is then outlined in the next section. We divide the presentation of the numerical results in Section 4 into three parts. In the first, as a check on the proposed numerical scheme, we compare the velocity profiles for oscillatory flow obtained numerically with the classical Womersley solution [32] in the case of a Newtonian fluid. Second, we discuss the behaviour of the components of the pressure gradient P'_M and P''_M that are in phase and $\pi/2$ out of phase with the volume flow rate, as the volume flow rate amplitude is varied. Tubes of three different radii are used in the simulations. Excellent agreement is found with experimental data [28] for a tube of radius $430\mu m$. Third, in an attempt to identify and interpret the non-Newtonian behaviour of our model blood under oscillatory flow conditions, comparisons of the velocity profiles are made with those of appropriately chosen Newtonian fluids. Finally, we seek to relate the macroscopic blood behaviour in different size tubes and at two different angular frequencies to the aggregate properties such as the average aggregate size and the cell number density.

2 A one-dimensional time-dependent model for blood

In Part I of this work Moyers-Gonzalez et al. [17] derived the governing equations for a new non-homogeneous model for the flow of human blood. The microstructure underlying this model was seen to consist of aggregates (rouleaux) of different sizes (so-called $j-$mers ($j = 1, 2, 3, \ldots$)) and made up of mutually attractive red blood cells. Each rouleau was represented by a Hookean dumbbell which was seen, at least for sufficiently small rates of deformation, to be capable of describing the deformation and displacement of real aggregates. Under general flow conditions and via binary reactions, the model permits the aggregates of dumbbells to fragment and coalesce and move within the fluid, the size and number density of these aggregates depending upon time, the local shear rate and wall effects.

2.1 Recapitulation of governing equations

Let N_0 denotes the cell number density and M the aggregate number density so that $n := N_0/M$ is the (local) average aggregate size. We denote the elastic

stress tensor due to all $k-$mers by $\boldsymbol{\tau}_k$. Therefore,

$$\boldsymbol{\tau} := \sum_{k=1}^{\infty} \boldsymbol{\tau}_k,$$

will denote the total elastic stress tensor, and takes into account the contribution of aggregates of all sizes to the total Cauchy stress tensor. We now introduce a tensor $\boldsymbol{\sigma}$, defined by

$$\boldsymbol{\sigma} := \sum_{k=1}^{\infty} \frac{\boldsymbol{\tau}_k}{k}.$$

With this notation in place, the equations describing the non-homogeneous blood model derived in [17] may be written as

$$\frac{DN_0}{Dt} = D_{tr}\nabla^2 N_0 - \frac{D_{tr}}{(k_B T + \kappa)}\nabla\nabla : \boldsymbol{\tau}, \tag{5}$$

$$\boldsymbol{\tau} + \bar{\mu}\, \overset{\triangledown}{\boldsymbol{\tau}} - D_{tr}\bar{\mu}(\nabla^2\boldsymbol{\tau} + (\nabla\nabla : \boldsymbol{\tau})\boldsymbol{\delta}) = N_0(k_B T + \kappa)\bar{\mu}\dot{\boldsymbol{\gamma}}, \tag{6}$$

$$\frac{DM}{Dt} = D_{tr}\nabla^2 M - \frac{D_{tr}}{(k_B T + \kappa)}\nabla\nabla : \boldsymbol{\sigma} - \frac{a(\dot{\gamma})}{2}M^2 + \frac{b(\dot{\gamma})}{2}(N_0 - M), \tag{7}$$

$$\boldsymbol{\sigma} + \bar{\mu}\, \overset{\triangledown}{\boldsymbol{\sigma}} - D_{tr}\bar{\mu}(\nabla^2\boldsymbol{\sigma} + (\nabla\nabla : \boldsymbol{\sigma})\boldsymbol{\delta}) = M(k_B T + \kappa)\bar{\mu}\dot{\boldsymbol{\gamma}}. \tag{8}$$

In (5)-(8) above, D_{tr} is a translational diffusivity and $\bar{\mu}$ is an averaged (shear-rate and time dependent) relaxation time. The functions a and b of the shear rate $\dot{\gamma}$, appearing in Eqn. (7), are chosen, respectively, as the rate at which an $(i+j)-$mer is formed from an $i-$mer and a $j-$mer, and the rate at which an $(i+j)-$mer breaks into an $i-$mer and a $j-$mer. A detailed description of these functions is supplied in Appendix A. k_B and T are, in the usual notation, respectively, the Boltzmann constant and the absolute temperature (in degrees K). $(k_B T+\kappa)$ therefore consists of the sum of a very small Brownian contribution and a constant κ, the latter intended to take account of impacts of a rouleau with other blood cells. It may be seen that Eqn. (5) is analogous, for example, to the equation (34) derived in [2] for the polymer chain number density for a suspension of Hookean dumbbells. Eqn. (6) is a generalized (non-homogeneous and parabolic) Oldroyd-B type constitutive equation.

To close the system of equations for $(\boldsymbol{v}, p, N_0, M, \boldsymbol{\sigma}, \boldsymbol{\tau})$ we must add the usual equation of conservation of linear momentum and the incompressibility constraint:

$$\rho_f \frac{D\boldsymbol{v}}{Dt} = -\nabla p + \eta_N \nabla^2 \boldsymbol{v} + \nabla \cdot \boldsymbol{\tau}, \tag{9}$$

$$\nabla \cdot \boldsymbol{v} = 0, \tag{10}$$

where ρ_f denotes the fluid density, p the pressure and η_N is the constant plasma viscosity.

2.1.1 Non-dimensionalization and dimensionless groups

We non-dimensionalize Eqns. (5)-(10) by rescaling the variables as follows:

$$\hat{N}_0 = \frac{N_0}{N_{av}}, \quad \hat{M} = \frac{M}{N_{av}}, \quad \hat{p} = \frac{p}{N_{av}(k_B T + \kappa)}, \quad \hat{t} = \frac{tV}{R},$$
$$\hat{\boldsymbol{x}} = \frac{\boldsymbol{x}}{R}, \quad \hat{\boldsymbol{v}} = \frac{\boldsymbol{v}}{V}, \quad \hat{\boldsymbol{\tau}} = \frac{\boldsymbol{\tau}}{N_{av}(k_B T + \kappa)}, \quad \hat{\boldsymbol{\sigma}} = \frac{\boldsymbol{\sigma}}{N_{av}(k_B T + \kappa)},$$

where R denotes a characteristic length and V a characteristic flow speed (a maximum value, for example). N_{av} is the average number density of red cells, defined over a region $\mathcal{D} \subset \mathbb{R}^3$ by

$$N_{av} := \frac{1}{\mathrm{vol}\mathcal{D}} \int_{\mathcal{D}} N_0(\boldsymbol{x}, t)\, d\boldsymbol{x}. \tag{11}$$

For ease of notation we henceforth drop the hats on all dimensionless quantities. Let us introduce cylindrical polar coordinates (r, θ, z) and consider unsteady pressure-driven axisymmetric blood flow in a uniform pipe with axis in the z-direction, as shown in Figure A.1. Then, a solution to unsteady tube flow of the form $\boldsymbol{v} = (0, 0, v_z(r, t))$, $p = p(z, t)$ and all other variables functions of only r and t may be sought, leading to the following coupled system of equations:

$$\frac{\partial N_0}{\partial t} - \frac{1}{Pe}\frac{1}{r}\frac{\partial}{\partial r}\left(r\frac{\partial N_0}{\partial r}\right) + \frac{1}{Pe}\frac{1}{r}\frac{\partial}{\partial r}\left(r\frac{\partial \tau_{rr}}{\partial r}\right) = 0, \tag{12}$$

$$\frac{\partial M}{\partial t} - \frac{1}{Pe}\frac{1}{r}\frac{\partial}{\partial r}\left(r\frac{\partial M}{\partial r}\right) + \frac{1}{Pe}\frac{1}{r}\frac{\partial}{\partial r}\left(r\frac{\partial \sigma_{rr}}{\partial r}\right) + \frac{aN_0}{2n}M - \frac{b}{2}(N_0 - M) = 0, \tag{13}$$

$$De\frac{\partial \tau_{rr}}{\partial t} - \frac{De}{Pe}\left(\frac{2}{r}\frac{\partial}{\partial r}\left(r\frac{\partial \tau_{rr}}{\partial r}\right)\right) + \tau_{rr} = 0, \tag{14}$$

$$De\frac{\partial \tau_{rz}}{\partial t} - \frac{De}{Pe}\left(\frac{1}{r}\frac{\partial}{\partial r}\left(r\frac{\partial \tau_{rz}}{\partial r}\right) - \frac{\tau_{rz}}{r^2}\right) - (\tau_{rr} + N_0)De\frac{\partial v_z}{\partial r} + \tau_{rz} = 0, \tag{15}$$

$$De\frac{\partial \tau_{zz}}{\partial t} - \frac{De}{Pe}\left(\frac{1}{r}\frac{\partial}{\partial r}\left(r\frac{\partial \tau_{zz}}{\partial r}\right) + \frac{1}{r}\frac{\partial}{\partial r}\left(r\frac{\partial \tau_{rr}}{\partial r}\right)\right) - 2De\frac{\partial v_z}{\partial r}\tau_{rz} + \tau_{zz} = 0, \tag{16}$$

$$De\frac{\partial \sigma_{rr}}{\partial t} - \frac{De}{Pe}\left(\frac{2}{r}\frac{\partial}{\partial r}\left(r\frac{\partial \sigma_{rr}}{\partial r}\right)\right) + \sigma_{rr} = 0, \tag{17}$$

$$Re\frac{\partial v_z}{\partial t} - \eta\frac{1}{r}\frac{\partial}{\partial r}\left(r\frac{\partial v_z}{\partial r}\right) - \frac{1}{r}\frac{\partial}{\partial r}(r\tau_{rz}) + \frac{\partial p}{\partial z} = 0. \tag{18}$$

In writing out Eqns. (12)-(14) and (16)-(17) we have used the fact (see Moyers-Gonzalez et al. [17]) that $\tau_{rr} = \tau_{\theta\theta}$ and $\sigma_{rr} = \sigma_{\theta\theta}$. The dimensionless group

De that appears in Eqns. (14)-(17) is defined in terms of a Maxwell Deborah number De_∞ (see (21) below) as follows:

$$De := \frac{\bar{\mu}V}{R} = \frac{nDe_\infty}{1 + g_n nDe_\infty}, \tag{19}$$

where the dimensionless fragmentation rate coefficient g_n is defined as

$$g_n(\dot{\gamma}) := a(\dot{\gamma})M + b(\dot{\gamma})\frac{(n-1)}{2}. \tag{20}$$

The Maxwell Deborah number De_∞ is the same as that for a suspension of monomers:

$$De_\infty = \frac{\lambda_H V}{R}, \tag{21}$$

where λ_H is the Maxwell relaxation time. The definition of Pe is

$$Pe = \frac{VR}{D_{tr}}, \tag{22}$$

and represents a ratio of convective fluxes to diffusive fluxes. From (19) we see that De is a complicated function of the local shear rate. However, as $\dot{\gamma} \to \infty$ the aggregates break up and the aggregation rate goes to zero, so that $a \to 0$, $n \to 1$ and De tends towards De_∞. It was shown by Bhave et al. [3] and Moyers-Gonzalez et al. [17], for example, that the definitions of De_∞ and Pe allow one to write down the ratio De_∞/Pe as

$$\frac{De_\infty}{Pe} = \frac{\ell_0^2}{24R^2}, \tag{23}$$

where ℓ_0 is the equilibrium length of a Hookean dumbbell so that $(24De_\infty/Pe)^{1/2}$ is the relative magnitude of a microscopic length scale to a macroscopic length scale. Where this ratio is small, therefore, wall effects on the bulk flow are anticipated to be weak, although as shown by Moyers-Gonzalez and Owens [18] in Part II of this work they will still have an influence upon the solution throughout the flow domain, even along the axis of symmetry. A boundary layer of thickness $O(De_\infty/Pe)^{1/2}$ was predicted in [18]. The Reynolds number (Re) and dimensionless viscosity η appearing in (18) are given by

$$Re = \frac{\rho_f VRDe_\infty}{\eta_\infty} \quad \text{and} \quad \eta = \frac{\eta_N De_\infty}{\eta_\infty}, \tag{24}$$

where $\eta_\infty := N_{av}(k_B T + \kappa)\lambda_H$ is the contribution from the red cells to the infinite shear rate viscosity of blood.

In this paper, Eqns. (12)-(18) are solved subject to a prescribed pressure gradient $\partial p/\partial z$.

2.2 Boundary and initial conditions

The solution of (12)-(18) requires a suitable choice of initial and boundary conditions. In order to prescribe suitable stress boundary conditions on the solid wall we assume, as have other authors before us [3,6,22], that the connector vectors of the dumbbells there are all orientated in the z-direction. It then follows from the Kramers expression [13] for the elastic stress tensor that its value on the wall is given by

$$\boldsymbol{\tau} = N_0 Q_0^2 \boldsymbol{e}_z \boldsymbol{e}_z - N_0 \boldsymbol{\delta}, \tag{25}$$

where Q_0 is the length of a dumbbell divided by its equilibrium length and $\boldsymbol{e}_z$ is a unit vector in the z-direction. $\boldsymbol{\delta}$ is the identity tensor. We note at this point that since τ_{zz} is not required in order to calculate the other field variables, omitting it from our calculations obviates the necessity to estimate Q_0 and the boundary condition on the remaining components of $\boldsymbol{\tau}$ is just $\tau_{ij} = -N_0 \delta_{ij}$.

The remaining boundary conditions are fairly standard. Along $r = 0$ symmetry considerations lead to

$$\tau_{rz} = 0, \ \frac{\partial v_z}{\partial r} = 0, \ \frac{\partial \tau_{rr}}{\partial r} = 0, \ \frac{\partial \sigma_{rr}}{\partial r} = 0, \ \frac{\partial M}{\partial r} = 0, \tag{26}$$

whereas on the wall ($r = 1$) we impose a no-slip condition on the axial velocity and natural boundary conditions on N_0 and M:

$$v_z = 0, \ \frac{\partial N_0}{\partial r} = \frac{\partial \tau_{rr}}{\partial r}, \ \ \frac{\partial M}{\partial r} = \frac{\partial \sigma_{rr}}{\partial r}. \tag{27}$$

Finally, conservation of the number of dumbbells in any section of the tube requires that N_0 should satisfy the constraint

$$\int_0^1 N_0 r \, dr = \frac{1}{2}. \tag{28}$$

Initial conditions for all variables were obtained from the steady solution computed as described in Part I [17] of this work and driven by a steady pressure gradient equal to the negative pressure gradient amplitude of the present paper.

3 Numerical method

The system of equations (12)-(18) may be written in the form

$$\frac{\partial \boldsymbol{q}}{\partial t} - \boldsymbol{\mathcal{D}}(\boldsymbol{q}) - \boldsymbol{\mathcal{R}}(\boldsymbol{q}) = \boldsymbol{0},$$

where $\boldsymbol{q} := (N_0, M, \tau_{rr}, \tau_{rz}, \tau_{zz}, \sigma_{rr}, v_z, p)^T$ is the vector of unknowns and $\boldsymbol{\mathcal{D}}$ and $\boldsymbol{\mathcal{R}}$ represent the diffusion and reaction terms in (12)-(18), respectively.

Let a superscript "(k)" on a dependent variable denote its evaluation at time $t = k\Delta t$, where Δt is the magnitude of a single time step. If we discretise (12)-(18) in time and space then the simplest fractional step method for the resolution of this system of equations (see, for example, Tyson et al. [30]) is

1. Solve $\partial \boldsymbol{q}/\partial t = \boldsymbol{\mathcal{R}}(\boldsymbol{q})$ over one time step Δt with data $\boldsymbol{q}^{(k)}$ to obtain an intermediate field $\boldsymbol{q}^*$.
2. Solve $\partial \boldsymbol{q}/\partial t = \boldsymbol{\mathcal{D}}(\boldsymbol{q}^*)$ over one time step Δt with data $\boldsymbol{q}^*$ to obtain $\boldsymbol{q}^{(k+1)}$.

As pointed out by Tyson et al. [30], there is no reason at all why these two half steps shouldn't be carried out with different methods of discretisation. In the present paper, however, we choose to use an implicit Euler scheme for the temporal discretisation and a standard second order Galerkin finite element method for the discretization in space for both half steps. The truncation error for our scheme is therefore $O(\Delta t, (\Delta r)^2)$ where Δr denotes the size of a finite element. Second-order accuracy in time would be possible using a Strang-splitting scheme [26], for example, but this was not implemented in the present paper. No upwinding of any sort was found to be necessary because of the extra regularity brought to bear on the system of stress equations by the diffusion terms. To reduce the computing time we did not calculate τ_{zz} although this may be obtained at any time from (16). The time-discretised equations corresponding to the diffusion step may be now be written in the form

$$\frac{N_0^{(k+1)} - N_0^*}{\Delta t} - \frac{1}{Pe}\frac{1}{r}\frac{\partial}{\partial r}\left(r\frac{\partial N_0^{(k+1)}}{\partial r}\right) + \frac{1}{Pe}\frac{1}{r}\frac{\partial}{\partial r}\left(r\frac{\partial \tau_{rr}^{(k+1)}}{\partial r}\right) = 0, \qquad (29)$$

$$\frac{M^{(k+1)}-M^*}{\Delta t}-\frac{1}{Pe}\frac{1}{r}\frac{\partial}{\partial r}\left(r\frac{\partial M^{(k+1)}}{\partial r}\right)+\frac{1}{Pe}\frac{1}{r}\frac{\partial}{\partial r}\left(r\frac{\partial \sigma_{rr}^{(k+1)}}{\partial r}\right)=0, \tag{30}$$

$$\frac{\tau_{rr}^{(k+1)}-\tau_{rr}^*}{\Delta t}-\frac{1}{Pe}\left(\frac{2}{r}\frac{\partial}{\partial r}\left(r\frac{\partial \tau_{rr}^{(k+1)}}{\partial r}\right)\right)=0, \tag{31}$$

$$\frac{\tau_{rz}^{(k+1)}-\tau_{rz}^*}{\Delta t}-\frac{1}{Pe}\left(\frac{1}{r}\frac{\partial}{\partial r}\left(r\frac{\partial \tau_{rz}^{(k+1)}}{\partial r}\right)-\frac{\tau_{rz}^{(k+1)}}{r^2}\right)=0, \tag{32}$$

$$Re\frac{v_z^{(k+1)}-v_z^*}{\Delta t}-\eta\frac{1}{r}\frac{\partial}{\partial r}\left(r\frac{\partial v_z^{(k+1)}}{\partial r}\right)-\frac{1}{r}\frac{\partial}{\partial r}(r\tau_{rz}^{(k+1)})+\frac{\partial p}{\partial z}=0, \tag{33}$$

where the starred variables, coming from the system of reaction equations, are known explicitly and given by

$$N_0^*=N_0^{(k)}, \tag{34}$$

$$\tau_{rr}^*=\left(\frac{De^{(k)}}{De^{(k)}+\Delta t}\right)\tau_{rr}^{(k)}, \tag{35}$$

$$\tau_{rz}^*=\left(\frac{De^{(k)}}{De^{(k)}+\Delta t}\right)\tau_{rz}^{(k)}+\left(\frac{De^{(k)}\Delta t}{De^{(k)}+\Delta t}\right)(\tau_{rr}^*+N_0^*)\frac{dv_z^*}{dr}, \tag{36}$$

$$M^*=\left(\frac{4\Delta t n^{(k)}}{4n^{(k)}+2aN_0^{(k)}\Delta t+2n^{(k)}\Delta t b^{(k)}}\right)\left(\frac{M^{(k)}}{\Delta t}+\frac{b^{(k)}}{2}N_0^*\right), \tag{37}$$

$$\sigma_{rr}^*=\left(\frac{De^{(k)}}{De^{(k)}+\Delta t}\right)\sigma_{rr}^{(k)}, \tag{38}$$

$$v_z^*=v_z^{(k)}. \tag{39}$$

The spatially discretised equations (29)-(33) are solved subject to the boundary conditions (25)-(27) and the particle number constraint (28). The results presented in Section 4 were computed on a uniform finite element mesh with 100 elements (201 nodes) and with a time step $\Delta t = 0.01$.

4 Results

All results in this section have been computed for oscillatory flow driven by a sinusoidally varying dimensionless pressure gradient of the form

$$-\frac{\partial p}{\partial z}(z,t)=P_M(z)\cos\omega^* t, \tag{40}$$

where $P_M > 0$ is the (dimensionless) pressure gradient amplitude at z and $\omega^* := \omega\lambda_H/De_\infty$ is a dimensionless angular frequency. For the results presented in Sections 4.1 and and 4.3 we have chosen to fix

$$P_M=\frac{600R\lambda_H}{\eta_\infty}, \tag{41}$$

this value corresponding to a dimensional pressure gradient amplitude of $600Nm^{-3}$. The dimensional angular frequency ω has been allowed to vary in our simulations from a physiological value of $4\pi \text{rad}s^{-1}$ up to an unrealistic (but numerically demanding) $400\pi \text{rad}s^{-1}$. λ_H, the relaxation time for a single cell, was set equal to $0.005s$. With the exception of the tube radius, other parameter values are supplied in Appendix A.

4.1 Oscillatory Newtonian tube flow

In the Newtonian case the non-dimensional equation of motion (18) becomes

$$Re\frac{\partial v_z}{\partial t} = -\frac{\partial p}{\partial z} + \eta\frac{1}{r}\frac{\partial}{\partial r}\left(r\frac{\partial v_z}{\partial r}\right), \tag{42}$$

where

$$\eta = \frac{\eta_a De_\infty}{\eta_\infty},$$

is the dimensionless fluid viscosity and η_a is the fluid viscosity in dimensional units. By seeking a solution (v_z, p) to (42) of the form

$$v_z = \mathfrak{Re}\{\hat{v}_z(r)\exp(i\omega^* t)\},\ p = \mathfrak{Re}\{\hat{p}(z)\exp(i\omega^* t)\}, \tag{43}$$

it may be easily shown [32] that the solution to (42) is

$$v_z = \mathfrak{Re}\left\{\frac{1}{i\omega^* Re}\left(\frac{d\hat{p}}{dz}\right)\left(\frac{J_0\left(i^{3/2}r\alpha_a\right)}{J_0\left(i^{3/2}\alpha_a\right)} - 1\right)\exp(i\omega^* t)\right\}. \tag{44}$$

In (44) J_0 denotes the zeroth order Bessel function of the first kind and α_a is a Newtonian Womersley number, defined as

$$\alpha_a = R\sqrt{\frac{\rho_f \omega}{\eta_a}}. \tag{45}$$

In Figure A.2 we show the results of comparing the velocity profiles predicted using our numerical scheme for (42) and the exact solution (44) when $-d\hat{p}/dz = P_M = 600R\lambda_H/\eta_\infty$ (see (41)), the dimensional angular frequency $\omega = 400\pi \text{rad}s^{-1}$, the viscosity η_a is chosen equal to $0.005Pa.s$ and the tube radius $R = 430\mu m$. The high angular frequency was selected so as to make the comparison a more demanding exercise than it would have been otherwise and the numerical simulations were continued until periodicity had been attained according to some tolerance. The velocity profiles in both cases are shown at dimensional times $t = T/4,\ T/2,\ 3T/4$ and T, where $T = 5 \times 10^{-3}s$ is the period. The corresponding Reynolds number (see (24)) is $Re = 25.4553$ and the Womersley number is $\alpha_a = 6.9972$. Agreement between the two sets of results may be seen to be excellent at all times.

4.2 P'_M and P''_M vs U_M

We now suppose that corresponding to the sinusoidal pressure gradient input (40) we have a flow rate

$$U = 2\pi \int_{r=0}^{1} v_z(r,t) r \, dr,$$

that oscillates with the same angular frequency as $\partial p/\partial z$, albeit with a possible phase difference (see the remark below for a discussion of the validity of this assumption). We thus write U in the form

$$U = \mathfrak{Re}((U' + iU'') \exp(i\omega^* t)), \tag{46}$$

with real amplitudes U' and U''. Then, taking real parts of $((U'+iU'')\exp(i\omega^* t))$ we see that

$$\begin{aligned} U &= (U' \cos\omega^* t - U'' \sin\omega^* t), \\ &= \sqrt{U'^2 + U''^2} \left(\frac{U'}{\sqrt{U'^2 + U''^2}} \cos\omega^* t - \frac{U''}{\sqrt{U'^2 + U''^2}} \sin\omega^* t \right), \\ &= U_M \cos(\omega t + A). \end{aligned} \tag{47}$$

In (47) $U_M := \sqrt{U'^2 + U''^2}$ denotes the amplitude of the volume flow rate oscillations and A is the phase difference with the imposed pressure gradient, satisfying

$$\tan A = \frac{U''}{U'}.$$

Since we wish to compare our oscillatory flow results with those of Thurston [28] (who prescribed the velocity and then measured the pressure) we are interested in the components of the pressure gradient in phase and in quadrature with the volume flow rate. With this in view we write $-\partial p/\partial z$ in the complex form

$$-\frac{\partial p}{\partial z} = \mathfrak{Re}((P'_M + iP''_M) \exp(i(\omega t + A))), \tag{48}$$

and equate (40) and (48) to give

$$-\frac{\partial p}{\partial z} = P_M \cos\omega^* t = P'_M \cos(\omega^* t + A) - P''_M \sin(\omega^* t + A). \tag{49}$$

As explained in the Introduction, P'_M and P''_M are understood to be, respectively, the amplitudes of the oscillatory pressure gradient components in phase and in quadrature with the volume flow rate, and given by

$$P'_M = P_M \cos A, \;\; P''_M = -P_M \sin A. \tag{50}$$

To calculate P'_M and P''_M we first prescribe P_M and then solve (29)-(39) in $r \in (0,1)$, over some time interval taken to be sufficiently long that the volume flow rate becomes periodic in time and may be expressed in the form (47).

In [27], Thurston derived leading order expressions for P'_M and P''_M for a linear viscoelastic fluid. In terms of our non-dimensional variables these become

$$P'_M = \frac{8\eta' U_M}{\pi}, \tag{51}$$

and

$$P''_M = \frac{8U_M}{\pi}(-\eta'' + \alpha_b^2 De_\infty), \tag{52}$$

where η' and η'' are, respectively, the dimensionless dynamic viscosity and the dimensionless elastic component of the complex viscosity η^*. α_b is a viscoelastic Womersley number which, by analogy with the Newtonian case (45), is defined by

$$\alpha_b = R\sqrt{\frac{\rho_f \omega}{\eta_\infty}}. \tag{53}$$

From (51)-(52) we see that for a Newtonian fluid (where η' is the fluid viscosity, $\eta'' = 0$ and α_b in (52) should be replaced by α_a (45)) both P'_M and P''_M would be positive linear functions of U_M with graphs having positive slopes (see Fig.1 of [28] for graphs in the case of glycerol, for example).

In order to compare our results with those from the experiments of Thurston [28] we introduce (as did he) the root-mean-square (rms) values of U_M, P'_M and P''_M calculated over one period T. Denoting these, respectively, by Urms, P'rms and P''rms we get

$$U\text{rms} := \sqrt{\frac{1}{T}\int_0^T U_M^2 \cos^2\left(\frac{2\pi t}{T}\right)\, dt} = \frac{1}{\sqrt{2}}U_M \approx 0.707 U_M,$$

and, likewise, $P'\text{rms} := P'_M/\sqrt{2}$ and $P''\text{rms} := P''_M/\sqrt{2}$.

In Figs. A.3 and A.4 we show plots of P'rms and $|P''\text{rms}|$ against the rms volume flow rate amplitude Urms.

In Fig. A.3 the set of four upper curves correspond to the numerical predictions for tube radii of $R = 25\mu m$, $125\mu m$ and $430\mu m$ of P'rms, as well as Thurston's experimental determination of P'rms in the case of a tube of radius $430\mu m$. These radii were chosen so as to correspond in size to vessels that are somewhere between arterioles and small arteries in the human cardiovascular system and where blood flow is still pulsatile (see Table I of [5], for example). The four lower curves are those of $|P''\text{rms}|$. The $|P''\text{rms}|$ curves for $R = 25\mu m$ and $R = 125\mu m$ actually show $-P''$rms since P''rms is negative for the values of the rms volume rate over which the curves are plotted. In the final case ($R = 430\mu m$) both theoretical and experimental $|P''\text{rms}|$ curves appear to possess a sharp minimum. In fact this is a crossover point from $P''\text{rms} < 0$ (to the left of the minimum) to $P''\text{rms} > 0$ (to its right).

If we refer to Eqns. (50), (51) and (52) we understand that $P'\text{rms} > 0$ and

$P''\text{rms} < 0$ means that elastic effects are important enough that the sum of terms on the right-hand side of (52) is negative. At the same time we note from (50) that $A > 0$, so that the volume flow rate oscillation peaks and troughs occur before the corresponding extrema in the applied pressure gradient. In the case of the graphs of the rms in phase and in quadrature components of P_M for a tube of radius $430\mu m$, A passes from positive to negative at the point where $|P''\text{rms}|$ attains its minimum (at $U_{rms} = 1.554x10^{-}9$). Thus the volume flow rate oscillations go from preceding the corresponding pressure oscillations to lagging behind as viscous and inertial effects take over from those due to elasticity. The changes brought about in $P'\text{rms}$ as A passes from being small and positive to small in absolute value and negative are not as dramatic as in the case of $|P''\text{rms}|$. This is fairly easily explained by the fact that changes in A constitute a first order effect in $|P''\text{rms}|$ ($-P''_M \sim P_M A$ for small A) but a second order, largely negligible, effect in $P'\text{rms}$. The slight reduction in the gradient of $P'\text{rms}$ (the hydraulic resistance) as the volume flow rate amplitude increases is due to a small amount of shear thinning. Finally, from Fig. A.3 we observe that as the radii of the tubes increase from $25\mu m$ to $430\mu m$ the volume flow rate amplitude that results from a given applied pressure gradient amplitude also increases, as is to be expected, and results in a shift to the right of the corresponding $P'\text{rms}$ and $|P''\text{rms}|$ curves with increasing R.

In Fig. A.4 we show a zoom of the numerical results and measurements of Thurston [28] for $P'\text{rms}$ and $|P''\text{rms}|$ in a tube of radius $430\mu m$. Also shown are the numerical predictions of the homogeneous blood model of Fang and Owens [11], where all parameters were chosen as in the non-homogeneous model with the sole exception of the steady viscosity fitting parameter θ, for which best results were obtained with $\theta = 0.08s$. Although the two sets of numerically generated data are close to each other, as might be expected for a tube of this size (with $Pe = 32357.5$), the non-homogeneous predictions are closer to the experimental results than those of the homogeneous model and would seem to indicate that non-homogeneity still plays a small but non-negligible role in correctly predicting the relationship between the pressure and flow rate amplitudes. It should be noted here that the very close agreement obtained by Fang and Owens in [11] with the experimental data of Thurston [28] was only possible, for the parameters used in that paper, with a velocity slip boundary condition. In the present paper we observe that agreement of the homogeneous model results with those of Thurston [28] has not required such a slip condition, the reason being the choice of a lower (and more realistic) zero shear-rate polymeric viscosity η_0 (see Appendix A).

Remark From Eqns. (14), (15) and (18), the assumption that a time-periodic pressure gradient will result in a flow rate that is also periodic, with the same period (albeit with a possible phase shift), relies on the non-dimensional viscosity $N_0 De$ in (15) being independent of time, so that all variables may be

expressed in the form of a product of a complex amplitude and $\exp(i\omega^* t)$. We will see in the next Section that due to thixotropic effects and for the choice of model and flow parameters used in this paper, N_0De is a very weak function of time and that the assumption that U behaves as in Eqn. (47) becomes more and more reasonable as the Womersley number increases.

4.3 Viscoelastic vs Newtonian effects

Numerical simulations of oscillatory blood flow were performed using the scheme (29)-(39). Non-homogeneous effects on the velocity field and viscosity N_0De, as well as on the aggregate characteristics, are investigated by selecting the same three different values of the tube radius ($R = 25\mu m$, $125\mu m$ and $430\mu m$) as appeared in Section 4.2. The effect on the same variables of varying α_b (see (53)) is then studied by fixing the radius at $R = 430\mu m$ and choosing two different values for the angular frequency ($\omega = 4\pi \text{rad}s^{-1}$ and $\omega = 400\pi \text{rad}s^{-1}$). For all the tube radii considered, non-Newtonian effects are showcased by comparing the calculated velocity profiles with those of a Newtonian fluid having a viscosity chosen equal to the apparent viscosity of the model blood under steady Poiseuille flow conditions ($\omega = 0$) and $d\hat{p}/dz = -600R\lambda_H/\eta_\infty$ in the same tube. An apparent viscosity for oscillatory flow could have been defined as the viscosity of the Newtonian fluid which yields the same volume flow rate amplitude as the blood model at a given pressure gradient amplitude [7,15], but we thought it more enlightening to see how differences in the volume flow rate amplitudes of the model blood and Newtonian fluid developed in tubes of various radii. In Figs. A.5, A.7 and A.9 the non-Newtonian and Newtonian velocity profiles have been computed at times $t = 0, T/10, \ldots, 9T/10$ where $T = (2\pi/\omega)s$ is the period. We indicate in Fig. A.5 the time at which the various profiles were computed, the same pattern following for all the figures, with the notable difference in Figs. A.5(b) and A.7(b) that the Newtonian profiles at t and $T - t$ almost coincide, giving rise to only 6 obviously distinct profiles. This is because, in the case of the small and intermediate radius tubes, U'' in (47) is negligibly small (that is, $A \approx 0$) and the pressure and volume flow rate are very nearly in phase. The reader is referred to the discussion of the Newtonian velocity profile for small Womersley numbers at the start of Section 4.3.3 for further explanation of this point.

4.3.1 Time variation of aggregate characteristics and viscosity

We begin our discussion of the results presented in Figs. A.5-A.10 by first observing that despite the obvious variation of the velocity profiles (and, were we to show them, the total extra stress profiles) with time, very little obvi-

ous change can be observed in the variables N_0, M and N_0De over the time interval $[0, T]$. Such variation as there is in these variables becomes even less marked as the angular frequency is increased, and this may be seen most clearly by comparing the graphs of the non-dimensional viscosity N_0De in Figs. A.10 (d) and A.12 (d). The reason, at least for the choice of parameters employed in this paper and at the angular frequencies at which the experiments are performed, is the same as led to only small variations in n when the homogeneous model was used by Owens [20] in a time-dependent Couette flow and subjected to repeated triangular (sawtooth) variations of shear rate (see Fig. 7(b) of that paper): the variables that describe the state of the aggregates take time to react to changes in the local shear rate since both N_0 and M satisfy differential equations (see Eqns. (12) and (13)). Our model blood is thixotropic and, depending on the choice of material parameters, a sufficiently high oscillatory frequency will therefore result in only very small variations in N_0 and M (and thus in n and N_0De) once periodic conditions have been established. It is at this point that we highlight the inadequacy of generalized Newtonian models to describe time-dependent blood flow (indeed, any time-dependent non-Newtonian flow) since the viscosity will, in this case, be an explicit function of the local shear rate and therefore change instantaneously with it. Our assumption of a volume flow rate that oscillates at the same frequency as the applied pressure gradient in Section 4.2 was seen to depend on the non-dimensional viscosity being independent of time. In the light of the results in the subplots (d) of Figs. A.6-A.10 this may therefore be seen to be reasonable.

4.3.2 Radial variation of aggregate characteristics and viscosity

Comparing migration effects, as measured by the cell number density N_0 in subplots (c) of Figs. A.6-A.10, leads to the conclusion that, as may be expected, these are strongest in the smallest tube and weakest in that having the largest radius. Since the largest shear rates are those that are evaluated nearest the wall it is unsurprising that the average aggregate size is seen to be a monotonic decreasing function of radius for all the tubes, although because the aggregation rate $a(\dot{\gamma})$ is not a monotonic decreasing function of shear rate (see Fig. A.13) sufficiently small pressure gradient amplitudes can lead to a local maximum in n at some point away from the axis of symmetry. The viscosity depends on both cell number density and aggregate size and it is credible that it should also be a monotonic decreasing function of radius at all times.

The dimensional volume flow rate amplitude (U_d, say) increases from $3.96 \times 10^{-14} m^3 s^{-1}$ for the tube of radius $R = 25\mu m$ to $1.38 \times 10^{-9} m^3 s^{-1}$ for the largest diameter tube. A peak average shear rate $\dot{\gamma}_{av,max}$ for the three tubes may then be calculated as $U_d/(\pi R^3)$ and leads to the values shown in Table 1.

The largest peak average shear rate in therefore to be found in the largest tube although this may have been anticipated, given the extent to which the velocity profiles in Figs. A.5(a), A.7(a) and A.9(a) are flattened in the bulk flow and from noting the velocity maxima along the centreline in the three cases. One consequence of the high shear rates near the wall in the largest tube is that the average aggregate there only consists of between one and two cells. Starting with the tube of radius $430\mu m$, the trend that may be seen as the tube radius decreases to a certain point is that as wall shear rates correspondingly decrease the viscosity and average aggregate size there increase while simultaneously wall effects are "felt" to a greater and greater extent along the centreline and result in a decrease in both quantities at $r = 0$. However, for very small tubes (such as $R = 25\mu m$) the number density of cells is now so high that aggregate formation is encouraged and aggregate properties become more uniform. The wall viscosity and average aggregate size continue to increase with decreasing radius and the centreline values of n and N_0De, having attained a minimum at some intermediate value of R now start to increase (Fig. A.6(c) and (d)).

Although the peak average shear rate is largest in the largest tube, we also note from Table 1 that the greatest relative difference in the Newtonian and blood volume flow rate amplitudes is to be seen in this tube. This is thought to be because at any radial distance r the non-Newtonian fluid experiences lower shear rates than the values in steady flow over one cycle. Aggregates will tend to form and reduce the volume flow rate below that predicted by the Womersley theory. This effect is most pronounced in the largest tube since it is there that the shear rates differ most from those in steady flow.

4.3.3 Velocity profiles and steady apparent viscosity

At the smallest radius the blood velocity profile tends more to that of plug flow, slipping along on a cell depleted region near $r = 1$. For the Newtonian velocity profiles we see that for α_a sufficiently small that we can neglect terms of $O(\alpha_a^4)$ and smaller, the exact solution (44) may be written approximately as a sinusoidally varying quadratic function of r:

$$v_z \approx \frac{P_M \alpha_a^2}{4\omega Re}(1 - r^2)\cos\omega t. \tag{54}$$

Once larger angular frequencies are used, however, the expression (54) is no longer a good approximation to (44) and in Fig. A.11(b) (and in that of its non-Newtonian counterpart) we see the usual regions of backflow associated with large Womersley numbers and a reduction in the volume flow rate amplitude relative to the value at $\omega = 4\pi \text{rad} s^{-1}$.

The alert reader will note from Table 1 that the apparent viscosity η_a does not decrease monotonically with tube radius, as it did in the Part I paper [17]

and in seeming contradiction therefore with the earlier predicted behaviour. It should be added that the drop in apparent viscosity with tube radius in steady flows is experimentally observable and has been known in the literature at least since the early 1930's [10]. The reason for the discrepancy lies in the fact that in the present paper the pressure gradient ($d\hat{p}/dz = -600R\lambda_H/\eta_\infty$) driving the steady Poiseuille flow used to determine the apparent viscosity is smaller in magnitude than that in [17]. At sufficiently large values of P_M the tendency of aggregates to form and the apparent viscosity to increase in intermediate tubes (say, $R = 125\mu m$) is overcome by the average shear rates generated by the applied pressure difference. Experimentally, for very small tubes the apparent viscosity is seen to drop with decreasing tube radius because of the so-called Fåhraeus effect (drop in the dynamic hematocrit) [9] and the development of a plasma-rich slip layer near the wall as particles migrate towards the tube centre. Only the latter is taken account of in the present implementation of our model.

4.3.4 Effects of changes in angular frequency

Finally, we note from Figs. A.10 and A.12 that for a fixed tube radius a hundredfold increase in the oscillatory frequency has little effect upon the migration of the cells but does result in the break up of additional aggregates, leading to slightly lower values of n and smaller values of the viscosity N_0De. The reduction in time variation of N_0, M, n and N_0De over one cycle as ω increases from $4\pi \text{rad}s^{-1}$ to $400\pi \text{rad}s^{-1}$ has already been noted in Section 4.3.1.

$R\ (\mu m)$	25	125	430
$U_d\ (m^3s^{-1})$	3.96×10^{-14}	1.02×10^{-11}	1.38×10^{-9}
$U_{Nd}\ (m^3s^{-1})$	4.0004×10^{-14}	1.085×10^{-11}	1.605×10^{-9}
$\dot{\gamma}_{av,max}\ (s^{-1})$	0.8067	1.6621	5.5604
$\eta_a\ (Pa.s)$	0.0023	0.0053	0.005

Table 1
Dimensional volume flow rate amplitude U_d, Newtonian volume flow rate amplitude U_{Nd}, peak average shear rate $\dot{\gamma}_{av,max}$ and apparent viscosity η_a for tubes of radii $R = 25\mu m$, $125\mu m$ and $430\mu m$.

5 Conclusions

In this paper we have used a simple numerical method with a non-homogeneous constitutive model for blood to improve upon earlier simulations by Fang and

Owens [11] of oscillatory flow of blood in a straight rigid-walled tube. Agreement with experimental results in a tube of radius $430\mu m$ has been shown to be convincing and wall effects, such as particle migration, to be in evidence. For tubes of radii corresponding to those in the human cardiovascular system that are somewhere between small arteries and arterioles we have examined the velocity profiles at two different oscillation frequencies and sought to interpret the macroscopic behaviour of blood in terms of the underlying microstructure.

A Definition of the aggregation and disaggregation rate functions a and b and parameter values

A.1 Aggregation and disaggregation rates a and b of (13)

Motivated by the work of [19] and of [23] we choose aN_{av} before non-dimensionalization as follows:

$$a(\dot{\gamma})N_{av} = \begin{cases} a_{1,3}\dot{\gamma}^3 + a_{1,2}\dot{\gamma}^2 + a_{1,0} & \text{for } 0 \le \dot{\gamma} \le \dot{\gamma}_c, \\ a_{2,3}\dot{\gamma}^3 + a_{2,2}\dot{\gamma}^2 + a_{2,1}\dot{\gamma} + a_{2,0} & \text{for } \dot{\gamma}_c \le \dot{\gamma} \le \dot{\gamma}_{\max}, \\ 0 & \text{for } \dot{\gamma} > \dot{\gamma}_{\max}, \end{cases} \tag{A.1}$$

where

$$\begin{aligned} a_{1,0} &= 1, \\ a_{1,2} &= 3a_{1,0}/\dot{\gamma}_c^2, \\ a_{1,3} &= -2a_{1,0}/\dot{\gamma}_c^3, \end{aligned}$$

$$\begin{aligned} a_{2,0} &= \frac{2a_{1,0}\dot{\gamma}_{\max}^2(-\dot{\gamma}_{\max} + 3\dot{\gamma}_c)}{-\dot{\gamma}_{\max}^3 - 3\dot{\gamma}_{\max}\dot{\gamma}_c^2 + \dot{\gamma}_c^3 + 3\dot{\gamma}_c\dot{\gamma}_{\max}^2}, \\ a_{2,1} &= \frac{-12\dot{\gamma}_c a_{1,0}\dot{\gamma}_{\max}}{-\dot{\gamma}_{\max}^3 - 3\dot{\gamma}_{\max}\dot{\gamma}_c^2 + \dot{\gamma}_c^3 + 3\dot{\gamma}_c\dot{\gamma}_{\max}^2}, \end{aligned}$$

$$\begin{aligned} a_{2,2} &= \frac{6a_{1,0}(\dot{\gamma}_{\max} + \dot{\gamma}_c)}{-\dot{\gamma}_{\max}^3 - 3\dot{\gamma}_{\max}\dot{\gamma}_c^2 + \dot{\gamma}_c^3 + 3\dot{\gamma}_c\dot{\gamma}_{\max}^2}, \\ a_{2,3} &= \frac{-4a_{1,0}}{-\dot{\gamma}_{\max}^3 - 3\dot{\gamma}_{\max}\dot{\gamma}_c^2 + \dot{\gamma}_c^3 + 3\dot{\gamma}_c\dot{\gamma}_{\max}^2}. \end{aligned}$$

The critical shear rate $\dot{\gamma}_c$ is chosen as $\dot{\gamma}_c = 5.78s^{-1}$ (see [19]) and the maximum shear rate $\dot{\gamma}_{\max} = 900s^{-1}$. A graph of aN_{av} over $[\dot{\gamma}_c, \dot{\gamma}_{\max}]$ is shown in Fig. A.13 (a) and a zoom of the graph over $[0, \dot{\gamma}_c]$ in Fig. A.13 (b). Here we see that small

amounts of shear ($0 \leq \dot{\gamma} \leq \dot{\gamma}_c$) favour aggregation but that beyond the critical value $\dot{\gamma}_c$ the higher flow rates reduce the rate of aggregation. The aggregation rate at $\dot{\gamma} = 0$ is not zero since in this case thermal agitation encourages collisions and the formation of aggregates.

Before non-dimensionalization $b(\dot{\gamma})$ is determined from $a(\dot{\gamma})N_{av}$ from the relationship that holds in steady homogeneous flow (see Eqns (27) and (28) of [20]):

$$b(\dot{\gamma}) = \frac{a(\dot{\gamma})N_{av}}{n_s^{(o)}(n_s^{(o)} - 1)}, \tag{A.2}$$

where

$$n_s^{(o)} := \frac{\eta_{st}(\dot{\gamma})}{\eta_\infty}\left(1 + \frac{3}{2}a(\dot{\gamma})N_{av}\lambda_H\right), \tag{A.3}$$

is the steady homogeneous average aggregate size, and

$$\eta_{st}(\dot{\gamma}) = \eta_0\left(\frac{1 + \theta\dot{\gamma}^m}{1 + \beta\dot{\gamma}^m}\right),$$

with $\theta/\beta := \eta_\infty/\eta_0$, is the steady polymeric viscosity of Cross type ([8]), fitted to steady shear data. The non-dimensionalized forms of the aggregation and disaggregation functions, here denoted by $\hat{a}$ and $\hat{b}$, respectively, are related to a and b as follows:

$$\hat{a}(\hat{\dot{\gamma}}) := a(\dot{\gamma})N_{av}\frac{R}{V} \text{ and } \hat{b}(\hat{\dot{\gamma}}) := b(\dot{\gamma})\frac{R}{V},$$

where, as before, R is the tube radius and V is a characteristic velocity.

A.2 Parameter set

Physically realistic parameter values were chosen as follows:

- fluid density, $\rho_f = 1053.6kg.m^{-3}$,
- plasma viscosity, $\eta_N = 0.001Pa.s$,
- zero shear rate viscosity, $\eta_0 = 0.0326Pa.s$,
- high shear rate elastic viscosity, $\eta_\infty = 0.003Pa.s$,
- power law index $m = 1$,
- Cross model parameter $\theta = 1s^m$,
- Maxwell relaxation time, $\lambda_H = 0.005s$,
- Maxwell Deborah number $De_\infty = 1.4$.

Once the tube radius R is chosen, a characteristic velocity V may be calculated from $V = RDe_\infty/\lambda_H$ (see (21)).

References

[1] M. Anand and K. R. Rajagopal, A shear-thinning viscoelastic fluid model for describing the flow of blood, Int. J. Cardiovascular Medicine and Science 4 (2004), 59-68.

[2] A. N. Beris and V. G. Mavrantzas, On the compatibility between various macroscopic formalisms for the concentration and flow of dilute polymer solutions, J. Rheol. 38 (1994) 1235–1250.

[3] A. V. Bhave, R. C. Armstrong and R. A. Brown, Kinetic theory and rheology of dilute, non-homogeneous polymer solutions, J. Chem. Phys. 95 (1991) 2988–3000.

[4] P. J. Bronkhorst, G. J. Streekstra, J. Grimbergen, E. J. Nijhof, J. J. Sixma and G. J. Brakenhoff, A new method to study shape recovery of red blood cells using multiple optical trapping, Biophys J. 5 (1995) 1666-1673.

[5] C. G. Caro, T. J. Pedley, R. C. Schroter and W. A. Seed, The Mechanics of the Circulation, Oxford University Press, 1978.

[6] L. P. Cook and L. F. Rossi, Slippage and migration in models of dilute wormlike micellar solutions and polymeric fluids, J. Non-Newtonian Fluid Mech. 116 (2004) 347–369.

[7] N. A. Coulter Jr. and M. Singh, Frequency dependence of blood viscosity in oscillatory flow, Biorheology 8 (1971) 115–124.

[8] M. M. Cross, Rheology of non-Newtonian fluids: a new flow equation for pseudoplastic systems, J. Colloid Sci. 20 (1965) 417–437.

[9] R. Fåhraeus, The suspension stability of the blood, Physiol. Rev. 9 (1929) 241–274.

[10] R. Fåhraeus and T. Lindqvist, The viscosity of the blood in narrow capillary tubes, Am. J. Physiol. 96 (1931) 562–568.

[11] J. Fang and R. G. Owens, Numerical simulations of pulsatile blood flow using a new constitutive model, Biorheology 43 (2006) 637–660.

[12] D. L. Fry, D. M. Griggs and J. C. Greenfield, In vivo studies of pulsatile blood flow: The relationship of the pressure gradient to the blood velocity. In: E. O. Attinger (ed.), Pulsatile Blood Flow. McGraw-Hill, New York, 1964.

[13] H. A. Kramers, Het gedrag van macromoleculen in een stroomende vloeistof, Physica 11 (1944) 1–19.

[14] D. N. Ku, Blood flow in arteries, Annu. Rev. Fluid Mech. 29 (1997) 399-434.

[15] A. L. Kunz and N. A. Coulter, Non-Newtonian behavior of blood in oscillatory flow, Biophysical J. 7 (1967) 25–36.

[16] S. W. Lee and D. A. Steinman, On the relative importance of rheology for image-based CFD models of the carotid bifurcation, J. Biomed. Engrg. - Trans. ASME 129 (2007) 273–278.

[17] M. Moyers-Gonzalez, R. G. Owens and J. Fang, A non-homogeneous constitutive model for human blood. Part I: Model derivation and steady flow (2008), under review.

[18] M. Moyers-Gonzalez and R. G. Owens, A non-homogeneous constitutive model for human blood. Part II: Asymptotic solution for large Péclet numbers (2008), under review.

[19] T. Murata and T. W. Secomb, Effects of shear rate on rouleau formation in simple shear flow, Biorheology 25 (1988) 113–122.

[20] R. G. Owens, A new microstructure-based constitutive model for human blood, J. Non-Newtonian Fluid Mech. 140 (2006) 57–70.

[21] K. R. Rajagopal and A. R. Srinivasa, A thermodynamic framework for rate-type fluid models, J. Non-Newtonian Fluid Mech. 88 (2000) 207–227.

[22] L. F. Rossi and G. McKinley and L. P. Cook, Slippage and migration in Taylor-Couette flow of a model for dilute wormlike micellar solutions, J. Non-Newtonian Fluid Mech. 136 (2006) 79–92.

[23] T. Shiga, K. Imaizumi, N. Harada and M. Sekiya, Kinetics of rouleaux formation using TV image analyzer. I. Human erythrocytes, Am. J. Physiol. 245 (1983) H252–H258.

[24] D. A. Steinman and C. A. Taylor, Flow imaging and computing: large artery hemodynamics, Ann. Biomed. Engrg. 33 (2005) 1704–1709.

[25] J. F. Stoltz and M. Lucius, Viscoelasticity and thixotropy of human blood, Biorheology 18 (1981) 453–473.

[26] G. Strang, On the construction and comparison of difference schemes, SIAM J. Numer. Anal. 5 (1968) 506–517.

[27] G. B. Thurston, Theory of oscillation of a viscoelastic fluid in a circular tube, J. Acoust. Soc. Am. 24 (1960) 210-213.

[28] G. B. Thurston, Elastic effects in pulsatile blood flow, Microvasc. Res. 9 (1975), 145-157.

[29] G. B. Thurston, The viscosity and viscoelasticity of blood in small diameter tubes, Microvasc. Res. 11 (1976) 133–146.

[30] R. Tyson, L. G. Stern and R. J. LeVeque, Fractional step methods applied to a chemotaxis model, J. Math. Biol. 41 (2000) 455–475.

[31] G. Vlastos, D. Lerche and B. Koch, The superposition of steady on oscillatory shear and its effect on the viscoelasticity of human blood and a blood-like model fluid, Biorheology 34 (1997) 19-36.

[32] J. R. Womersley, Method for the calculation of velocity, rate of flow and viscous drag in arteries when the pressure gradient is known, J. Physiol. 127 (1955) 553–563.

[33] J. R. Womersley, An Elastic Tube Theory of Pulse Transmission and Oscillatory Flow in Mammalian Arteries, Wright Air Development Center Technical Report WADC TR (1957) 56-614.

[34] K. K. Yeleswarapu, Evaluation of Continuum Models for Characterizing the Constitutive Behavior of Blood, PhD thesis, University of Pittsburgh, Pittsburgh, PA 1996.

[35] K. K. Yeleswarapu, M. V. Kameneva, K. R. Rajagopal and J. F. Antaki, The flow of blood in tubes: theory and experiment, Mech. Res. Comm. 25 (1998), 257-262.

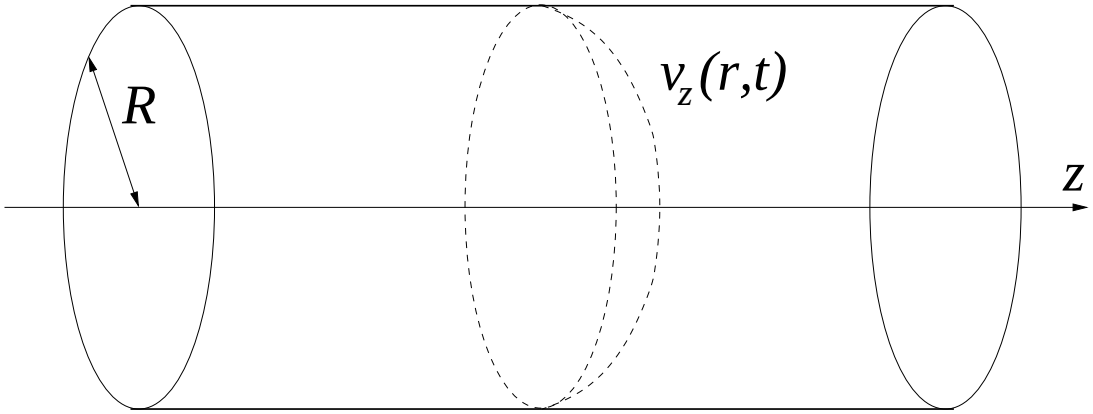

Fig. A.1. Diagrammatic representation of axisymmetric tube flow in a pipe of radius R.

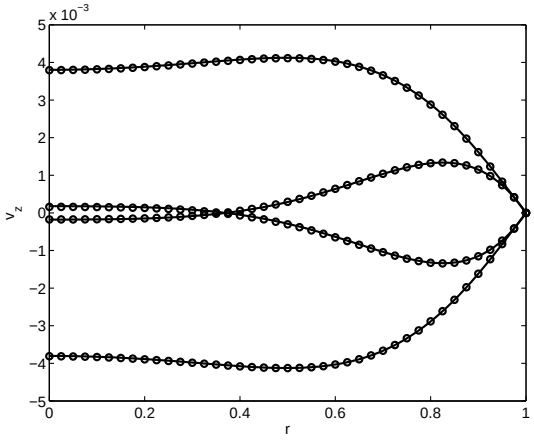

Fig. A.2. Numerical $(-)$ and exact $(\circ)$ (44) solutions for rapidly oscillating Newtonian profiles. Evaluation, from top to bottom at, say, $r = 0.8$ is at $t = 0,\ T/4,\ 3T/4$ and $T/2$. $\omega = 400\pi \mathrm{rad}s^{-1}$, $\eta_a = 0.005Pa.s$, $R = 430\mu m$, $Re = 25.4553$ and $\alpha_a = 6.9972$

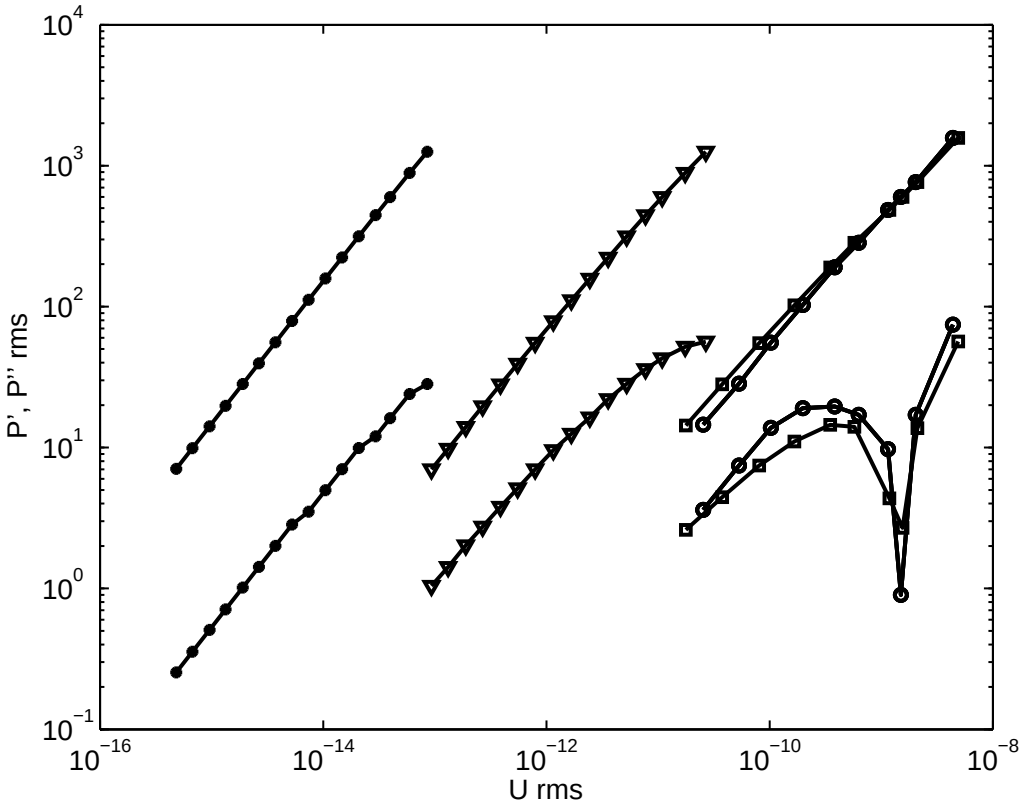

Fig. A.3. P'rms and $|P''$rms$|$ vs Urms for different radii. $\omega = 4\pi \text{rad} s^{-1}$. o− Thurston's [28] data, •− $R = 25\mu$m, ▼− $R = 125\mu$m and □− $R = 430\mu$m.

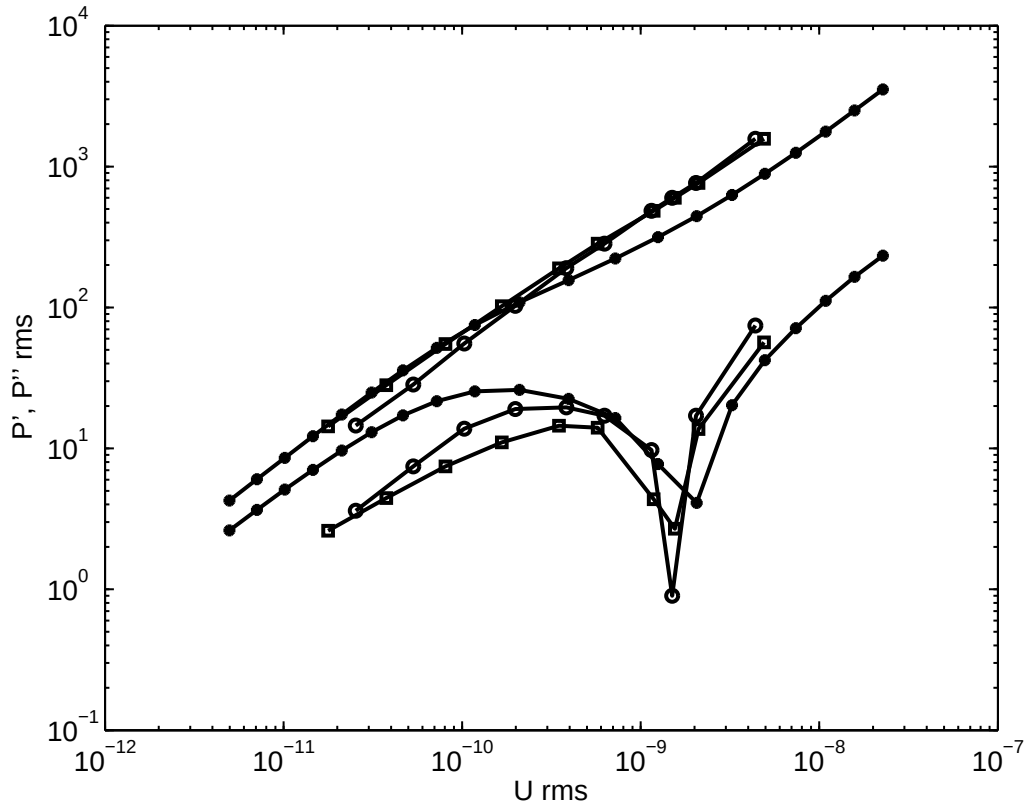

Fig. A.4. P'rms and $|P''$rms$|$ vs Urms. Comparison between homogeneous, nonhomogeneous and experimental data. $\omega = 4\pi \text{rad} s^{-1}$. o− Thurston's [28] data, •− $R = 430\mu$m homogeneous model and □− $R = 430\mu$m non-homogeneous model.

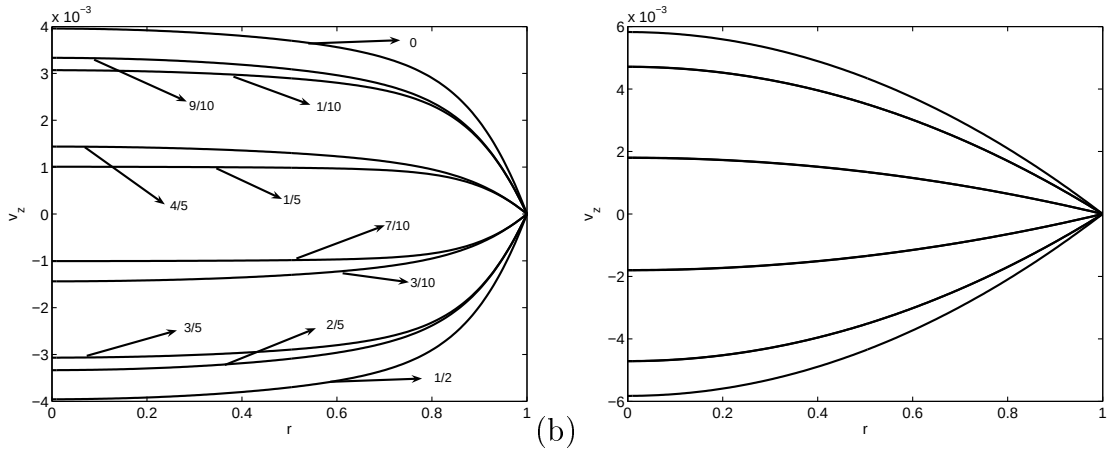

Fig. A.5. $\omega = 4\pi \text{rad} s^{-1}$ and $R = 25\mu m$. (a) Blood velocity; (b) Newtonian fluid velocity profiles at times $t = 0, T/10, \ldots, 9T/10$. $\eta_a = 0.0023 Pa.s$, $Re = 0.0860$, $Pe = 109.375$, $\alpha_b = 0.0525$ and $\alpha_a = 0.0600$.

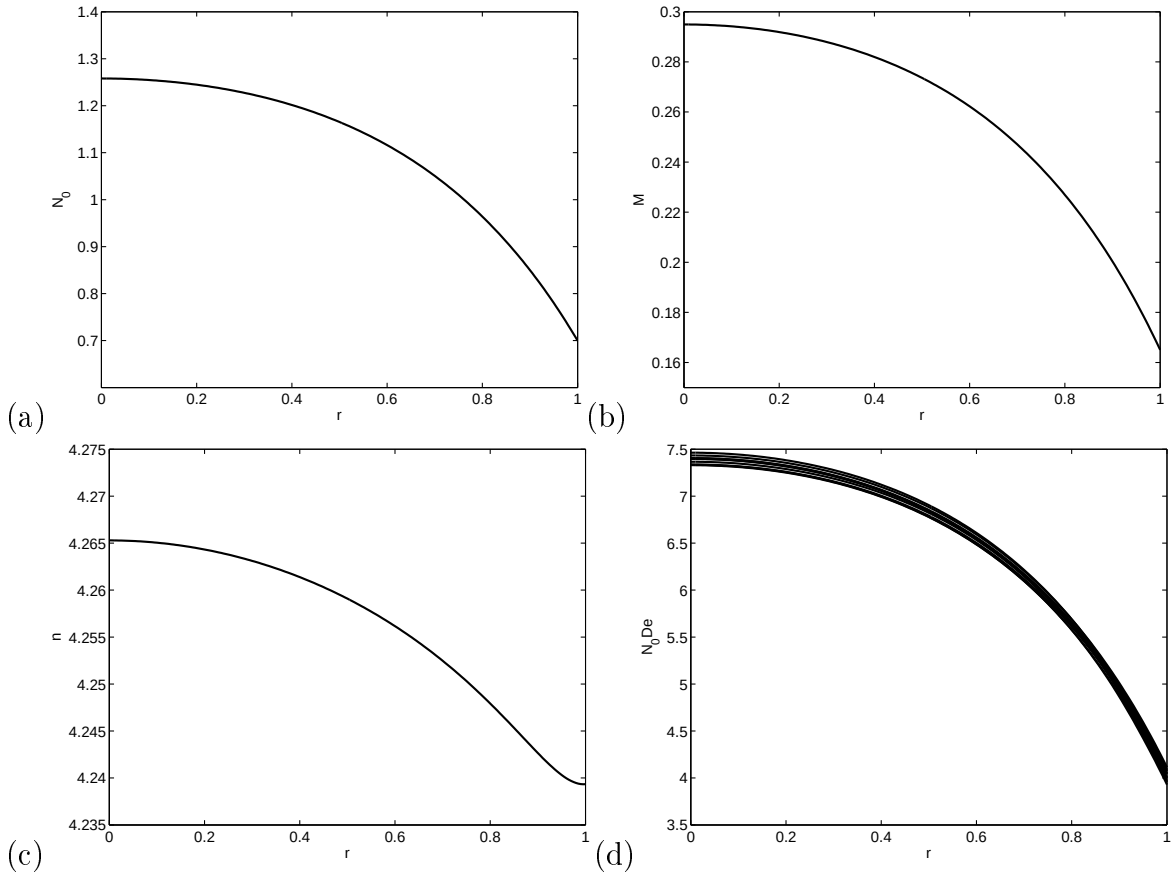

Fig. A.6. $\omega = 4\pi \text{rad} s^{-1}$ and $R = 25\mu m$. (a) $N_0(r,t)$; (b) $M(r,t)$; (c) $n(r,t)$; (d) $N_0(r,t)De(r,t)$ at times $t = 0, T/10, \ldots, 9T/10$. $\eta_a = 0.0023 Pa.s$, $Re = 0.0860$, $Pe = 109.375$, $\alpha_b = 0.0525$ and $\alpha_a = 0.0600$.

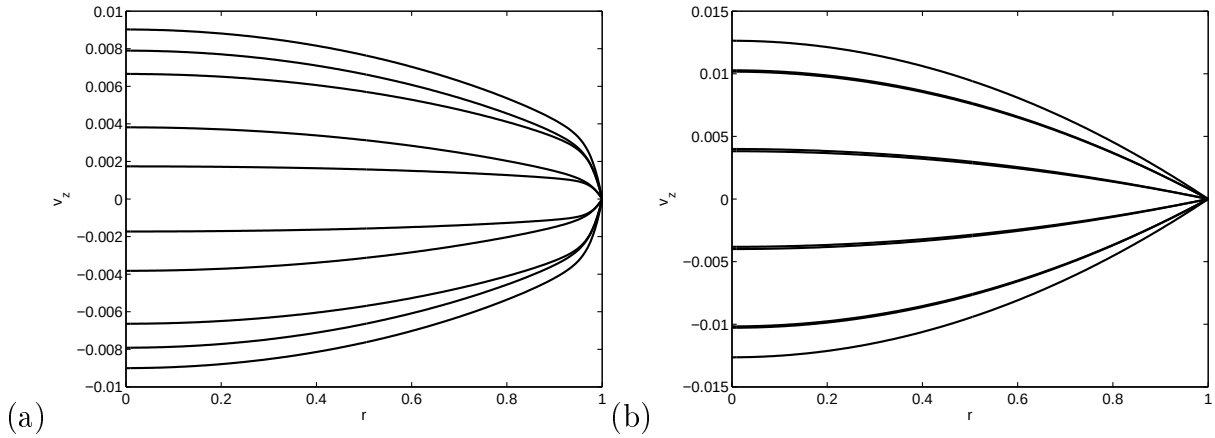

Fig. A.7. $\omega = 4\pi \text{rad} s^{-1}$ and $R = 125\mu m$. (a) Blood velocity; (b) Newtonian fluid velocity at times $t = 0, T/10, \ldots, 9T/10$. $\eta_a = 0.0053 Pa.s$. $Re = 2.1511$, $Pe = 2734.375$, $\alpha_b = 0.2626$ and $\alpha_a = 0.1976$.

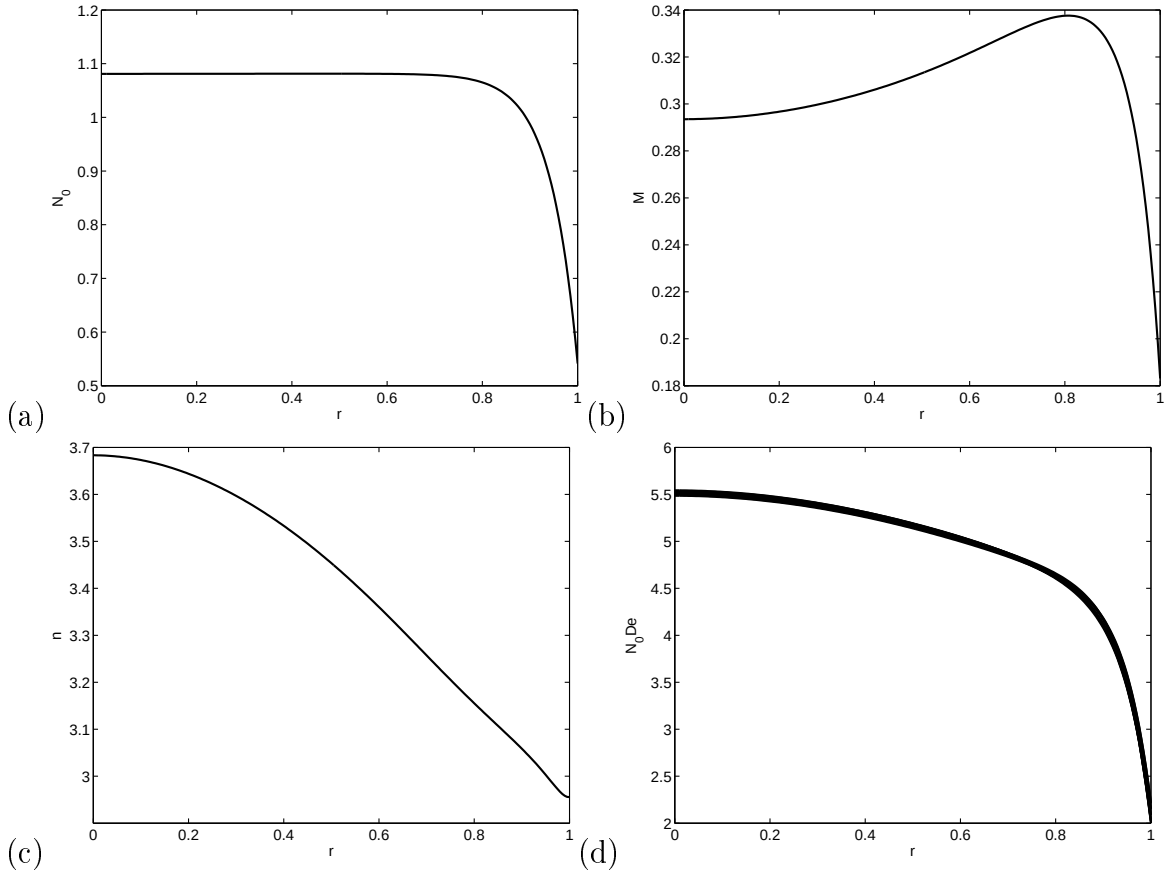

Fig. A.8. $\omega = 4\pi \text{rad} s^{-1}$ and $R = 125\mu m$. (a) $N_0(r,t)$; (b) $M(r,t)$; (c) $n(r,t)$; (d) $N_0(r,t)De(r,t)$ at times $t = 0, T/10, \ldots, 9T/10$. $\eta_a = 0.0053 Pa.s$, $Re = 2.1511$, $Pe = 2734.375$, $\alpha_b = 0.2626$ and $\alpha_a = 0.1976$.

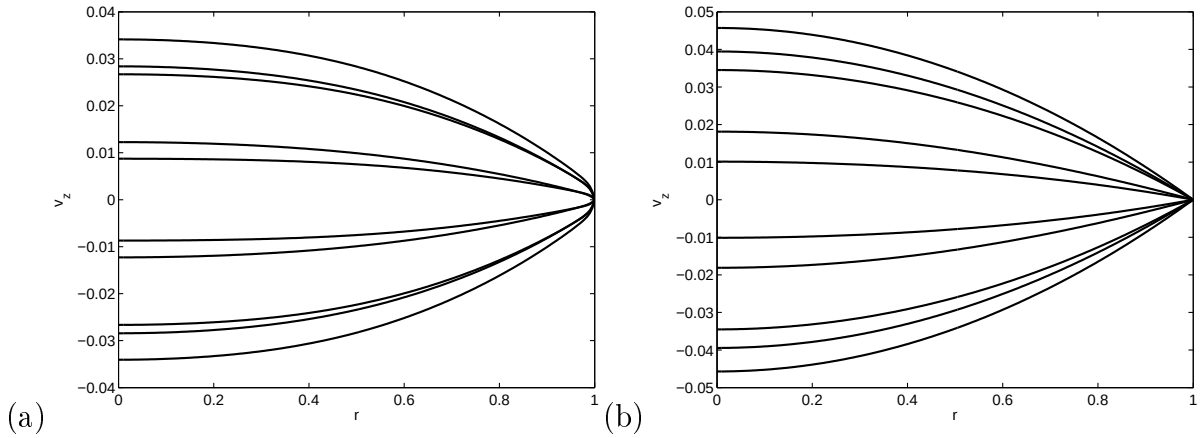

Fig. A.9. $\omega = 4\pi \text{rad} s^{-1}$ and $R = 430\mu m$. (a) Blood velocity; (b) Newtonian fluid velocity at times $t = 0, T/10, \ldots, 9T/10$. $\eta_a = 0.005 Pa.s$, $Re = 25.4553$, $Pe = 32357.5$, $\alpha_b = 0.9033$ and $\alpha_a = 0.6997$.

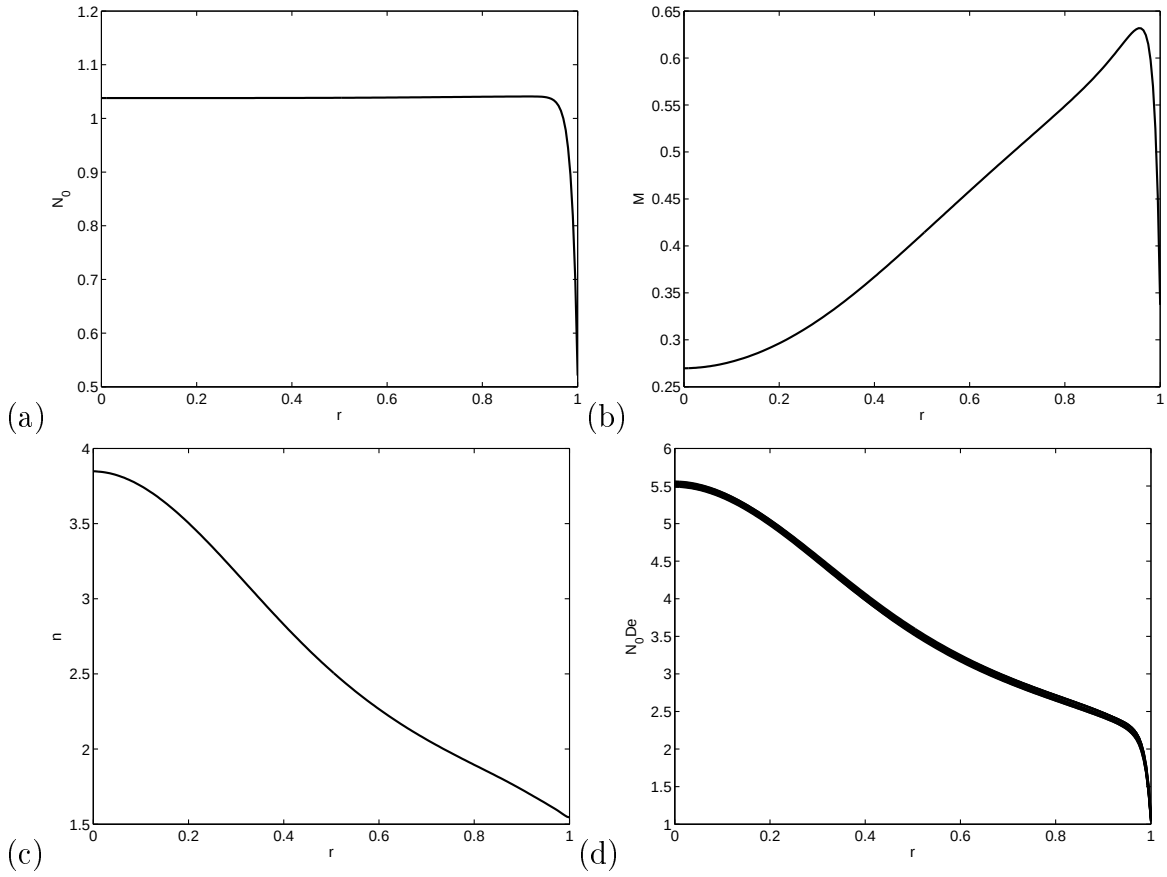

Fig. A.10. $\omega = 4\pi \text{rad} s^{-1}$ and $R = 430\mu m$. (a) $N_0(r,t)$; (b) $M(r,t)$; (c) $n(r,t)$; (d) $N_0(r,t)De(r,t)$ at times $t = 0, T/10, \ldots, 9T/10$. $\eta_a = 0.005 Pa.s$, $Re = 25.4553$, $Pe = 32357.5$, $\alpha_b = 0.9033$ and $\alpha_a = 0.6997$.

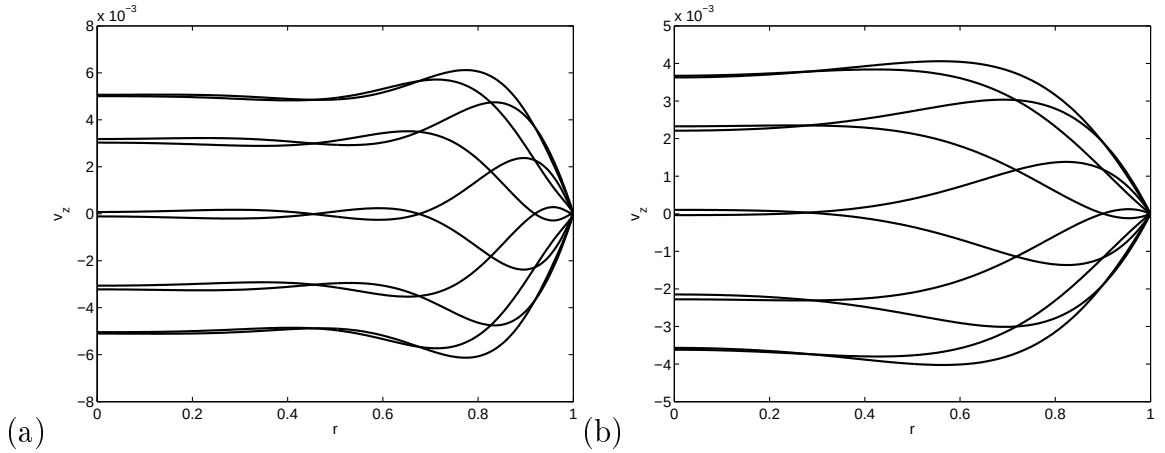

Fig. A.11. $\omega = 400\pi \text{rad} s^{-1}$ and $R = 430\mu m$. (a) Blood velocity; (b) Newtonian fluid velocity at times $t = 0, T/10, \ldots, 9T/10$. $\eta_a = 0.005 Pa.s$, $Re = 25.4553$, $Pe = 32357.5$, $\alpha_b = 9.0333$ and $\alpha_a = 6.9972$.

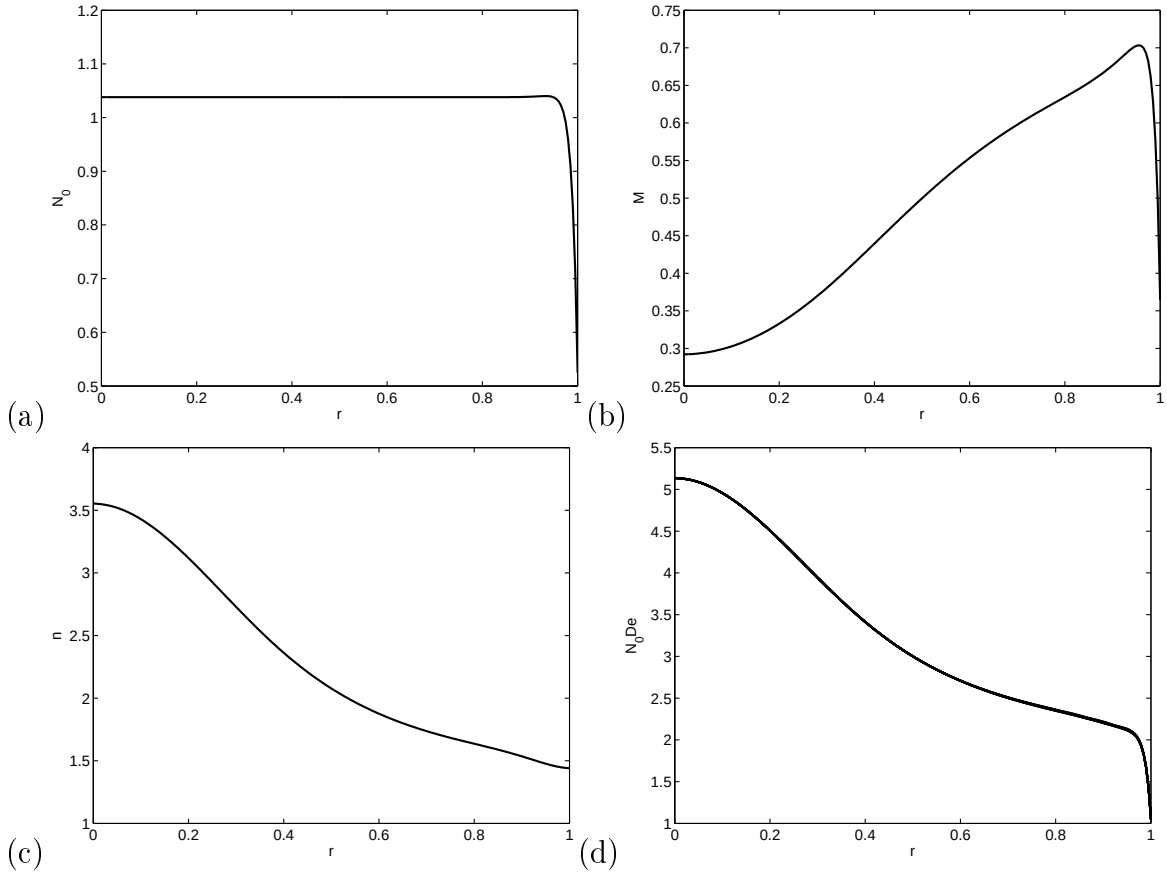

Fig. A.12. $\omega = 400\pi \text{rad} s^{-1}$ and $R = 430\mu m$. (a) $N_0(r,t)$; (b) $M(r,t)$; (c) $n(r,t)$; (d) $N_0(r,t)De(r,t)$ at times $t = 0, T/10, \ldots, 9T/10$. $\eta_a = 0.005 Pa.s$, $Re = 25.4553$, $Pe = 32357.5$, $\alpha_b = 9.0333$ and $\alpha_a = 6.9972$.

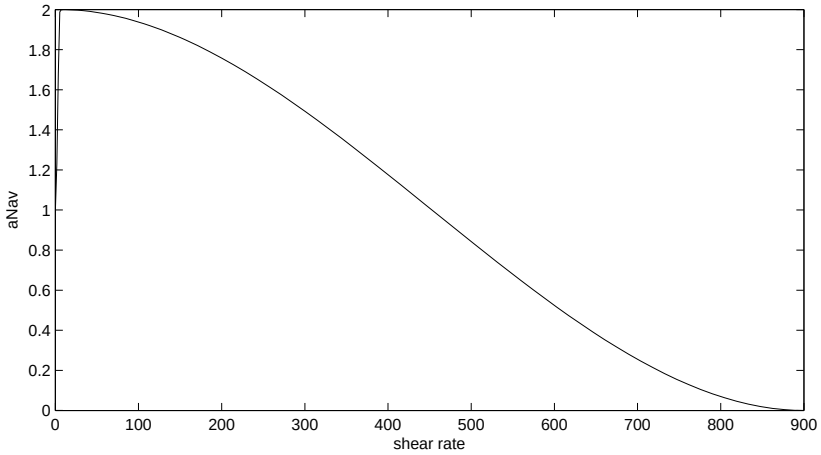

(a)

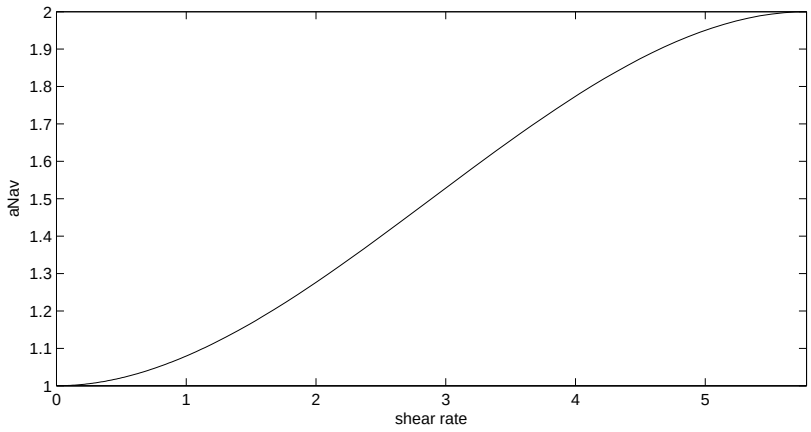

(b)

Fig. A.13. (a) The aggregation rate function $a(\dot{\gamma})N_{av}$ (A.1) over $[0, 900s^{-1}]$ (b) Zoom of $a(\dot{\gamma})N_{av}$ over $[0, 6s^{-1}]$